

Continuity equation for the flow of Fisher information in wave scattering

Received: 10 August 2023

Accepted: 19 April 2024

Published online: 10 June 2024



Jakob Hüpfl^{1,4}, Felix Russo^{1,4}, Lukas M. Rachbauer¹, Dorian Bouchet², Junjie Lu³, Ulrich Kuhl³✉ & Stefan Rotter¹✉

Using waves to explore our environment is a widely used paradigm, ranging from seismology to radar technology, and from biomedical imaging to precision measurements. In all these fields, the central aim is to gather as much information as possible about an object of interest by sending a probing wave at it and processing the information delivered back to a detector. Here we demonstrate that an electromagnetic wave scattered at an object carries locally defined and conserved information about all of the object's constitutive parameters. Specifically, we introduce the density and flux of Fisher information for general types of wave fields and identify the corresponding sources and sinks of information through which all these new quantities satisfy a fundamental continuity equation. We experimentally verify our theoretical predictions by studying a movable object embedded in a disordered environment and by measuring the corresponding Fisher information flux at microwave frequencies. Our results improve the understanding of the generation and propagation of information and open up possibilities for tracking and designing the flow of information even in complex environments.

One of the fundamental concepts in electromagnetism is the Poynting vector, introduced by John Henry Poynting¹ almost 140 years ago to describe the flow of energy carried by electromagnetic radiation. This quantity is intrinsically linked to the Poynting theorem, describing a local formulation of energy conservation with numerous applications in science and engineering^{2–6}. Electromagnetic fields do, however, not only carry energy but also gather information about the environment through which they travel or from which they are reflected. This property is heavily used in radar technology⁷, imaging^{8,9} and high-precision experiments^{10,11}, where information is acquired through the interaction between radiation and matter. One of the most crucial tasks in all of these applications is to collect as much information as possible about an object of interest to estimate its defining features, such as its position^{12,13}, its mass¹⁴ or its shape^{7,15} in the most precise way possible.

The fundamental quantity that provides the link between a measurable observable and the ultimate estimation precision is the so-called Fisher information (FI), which quantifies the amount of information

a signal contains about a certain parameter of interest¹⁶. Specifically, the Cramér–Rao bound states that the estimation precision is fundamentally limited by the inverse FI. Based on this fundamental insight, the concept of FI has been applied to numerous problems ranging from microscopy^{12,17–19} to complex scattering problems^{20–22}. To increase the precision of measurements, much effort has been dedicated to the optimal extraction of information from a given output signal^{17,23} and to the optimal shaping of an input field to maximize the amount of FI delivered to a detector^{20,24,25}. Although the input and output channels of such scattering problems have, thus, already been studied in terms of their potential to maximize the accessible information, little is known about the creation of FI at an object of interest and its propagation through the environment that this object may be embedded in.

Here we open the lid of this black box and investigate how electromagnetic fields acquire FI by interacting with a target and how they deliver it to the far field even in complex scattering systems. A key aspect of our proposed theoretical framework is that we assign to the

¹Institute for Theoretical Physics, Vienna University of Technology (TU Wien), Vienna, Austria. ²LIPhy, Université Grenoble Alpes, CNRS, Grenoble, France.

³Institut de Physique de Nice (INPHYNI), Université Côte d'Azur, CNRS, Nice, France. ⁴These authors contributed equally: Jakob Hüpfl, Felix Russo.

✉e-mail: ulrich.kuhl@univ-cotedazur.fr; stefan.rotter@tuwien.ac.at

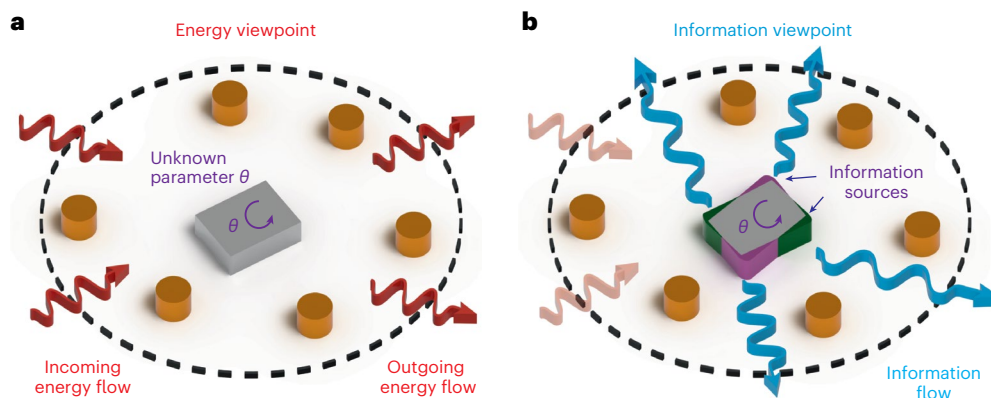


Fig. 1 | Illustration of precision measurements in complex systems. a. From the energy viewpoint, a scattering region containing cylindrical and rectangular scatterers is illuminated by coherent light, providing an incoming flow of energy (red incoming arrows). The parameter θ (here the angular orientation of the rectangular scatterer) is estimated from the outgoing energy flow (red outgoing arrows). **b.** In the alternative information viewpoint presented here, FI on a

specific parameter θ is created in those areas that change with varying θ . The corresponding areas at the corners of the rectangle, which the particle is moving towards (away from), when the parameter θ is increased, are coloured in purple (green). The information flows associated with these information sources are indicated by the blue outgoing arrows.

scattered electromagnetic field a local FI content at any point in space, in analogy to the energy density. Correspondingly, we demonstrate that also the flow of FI is described by a vectorial flux field, in analogy to the Poynting vector for the flow of energy. This FI flux directly originates from a target object (which acts as an information source), and is conserved during propagation away from the said object. Formally, this is expressed in terms of a continuity equation that preserves information in the same way as the Poynting theorem preserves energy. Using this framework, we provide a theoretical and experimental visualization of the FI flow through a complex scattering region. We emphasize the difference of this spatial information flow to earlier studies on the flow of quantum FI between a quantum system and its environment²⁶.

Spatial flow of information

To start out, we consider a scattering system made up of dielectric obstacles, which we probe with coherent electromagnetic waves (Fig. 1a shows a sketch of such a setup). The parameter θ characterizes a property of one or several constituents of the considered system, such as the size, shape or orientation of certain scatterers (Fig. 1a, grey rectangle), embedded here inside a disordered system (see the orange scatterers). This scenario occurs, for instance, in levitated optomechanics and particle-tracking experiments inside a complex scattering environment, where high-precision measurements of the particles' properties are necessary for accurate classification and analysis^{9,27–29}.

Our goal is to estimate a property of the target scatterer parameterized by θ (here the angular orientation of the target is shown in Fig. 1) by illuminating the system with a monochromatic electromagnetic wave (Fig. 1a, red incoming arrows) and by measuring (part of) the scattered wave (red outgoing arrows). Labelling the incoming and outgoing energy flux coefficients of the electromagnetic fields as \mathbf{c}^{in} and \mathbf{c}^{out} , respectively, allows us to describe this scattering process through the scattering matrix S , which connects these far-field patterns as follows: $\mathbf{c}^{\text{out}} = S\mathbf{c}^{\text{in}}$. The interaction of the field with the system during its propagation imprints information about the local system parameters on the outgoing field. However, the noise inherent in any signal (such as the photon shot noise inherent in coherent electromagnetic waves) limits the amount of information a wave can carry, requiring measurement schemes that maximize the extraction of information^{23,24,30}.

The relevant quantity that measures the amount of information on a specific parameter θ contained in a noisy signal is the so-called FI, namely, $\mathcal{F}(\theta) = \mathbb{E} \left(\left\{ \partial_{\theta} \ln[p(X; \theta)] \right\}^2 \right)$ (ref. 16). Here the noisy measure-

ment data are given by a random variable X with the corresponding probability distribution $p(X; \theta)$ and \mathbb{E} stands for the expectation value over the noise fluctuations. The importance of the FI is manifested in the Cramér–Rao inequality¹⁶, according to which the inverse of the FI sets a lower bound on the variance of any unbiased estimator $\hat{\theta}$ of θ based on the measurement data: $\text{Var} \hat{\theta} \geq \mathcal{F}(\theta)^{-1}$. To obtain high-precision estimates, signals with high FI are, thus, required.

Recent work has shown that in scattering problems, the rate of FI, $\mathcal{J}(\theta)$, delivered to the far field by a coherent monochromatic light field can be quantified by the following Hermitian FI operator $F = 4(\hbar\omega)^{-1} \partial_{\theta} S^{\dagger} \partial_{\theta} S$ (ref. 20). Specifically, this operator tells us that an input light field characterized by the coefficient vector \mathbf{c}^{in} contains the following rate of FI: $\mathcal{J}(\theta) = (\mathbf{c}^{\text{in}})^{\dagger} F \mathbf{c}^{\text{in}}$, which is reachable with a detection scheme based on shot-noise-limited photodetectors placed in the far field. The central question we will address in the following is how the FI operator can be extended to a local quantity describing the propagation of information in analogy to the energy flow.

To arrive at an expression for a corresponding FI flow from the FI operator F , we make use of the analogy to the well-known expressions for energy flow. In the far field, the total outgoing flow of energy is given by the Hermitian matrix $S^{\dagger}S$. This energy flux operator measures the flow of the outgoing wave energy in the asymptotic region as described by the Poynting vector (averaged over a time period)³¹:

$$\mathbf{S}^P = \text{Re}(\mathbf{E}_{\omega}^* \times \mathbf{H}_{\omega})/2, \quad (1)$$

where \mathbf{E}_{ω} and \mathbf{H}_{ω} are the complex amplitudes of the electric and magnetic fields at frequency ω , respectively. To formalize this connection between $S^{\dagger}S$ and \mathbf{S}^P , one considers the rate P of energy entering photodetectors of area A_i , located in the far field:

$$P = (\mathbf{c}^{\text{in}})^{\dagger} S^{\dagger} S \mathbf{c}^{\text{in}} = \sum_i \int_{A_i} \mathbf{S}^P \cdot \mathbf{n}_i, \quad (2)$$

where \mathbf{n}_i are the unit vectors normal to the detectors' surfaces.

To arrive at a corresponding relation for the rate of FI transfer $\mathcal{J}(\theta)$ (rather than for the energy) into the detectors, we transform the above equation (2) such that it contains the FI operator (Supplementary Section 1):

$$\mathcal{J}(\theta) = 4(\hbar\omega)^{-1} (\mathbf{c}^{\text{in}})^{\dagger} \partial_{\theta} S^{\dagger} \partial_{\theta} S \mathbf{c}^{\text{in}} = (\mathbf{c}^{\text{in}})^{\dagger} F \mathbf{c}^{\text{in}} = \sum_i \int_{A_i} \mathbf{S}^{\text{FI}} \cdot \mathbf{n}_i. \quad (3)$$

The formal analogy between equation (2) for the energy and equation (3) for the FI now allows us to identify the FI arriving at the detector surfaces as a corresponding (time-averaged) FI flux:

$$\mathbf{S}^{\text{FI}} = \frac{2}{\hbar\omega} \text{Re}(\partial_{\theta} \mathbf{E}_{\omega}^* \times \partial_{\theta} \mathbf{H}_{\omega}). \quad (4)$$

A sketch of this information flux is shown in Fig. 1b (blue arrows), which is defined by equation (4) as a vector field assigned to the electromagnetic field not only in the asymptotic region but in all of space—just like the Poynting vector for energy. In analogy to the Poynting theorem, we can also formulate a continuity equation for the FI flux of the following form:

$$\nabla \cdot \mathbf{S}^{\text{FI}} = \sigma^{\text{FI}}, \quad (5)$$

which allows us to identify the sources and sinks of information σ^{FI} . In the case of static isotropic dielectrics with permittivity function $\epsilon(\mathbf{r})$, these sources are given by $\sigma^{\text{FI}} = 2\hbar^{-1} \text{Im}[(\partial_{\theta} \epsilon) \mathbf{E}_{\omega}^* \cdot \partial_{\theta} \mathbf{E}_{\omega}]$ (similar sources need to be added if free charges or magnetic materials are present (Supplementary Section 2)). The sign of σ^{FI} determines, whether FI is created (+) or annihilated (−), and the above relation for σ^{FI} allows us to identify the quantity $-4i\hbar^{-1}(\partial_{\theta} \epsilon) \mathbf{E}_{\omega}$ as an effective electric current density $\mathbf{J}_{\text{eff}}^{\epsilon}$, oscillating with the frequency ω of the incoming driving field. Instead of radiating or annihilating energy (like an antenna), this effective current density radiates or annihilates FI in regions, where the incoming light field overlaps with those parts of matter that are sensitive to the parameter θ of interest (coloured areas near the corners of the target shown in Fig. 1b). Although the sign of $\partial_{\theta} \epsilon$ does not uniquely determine the sign of σ^{FI} , the positive/negative values of $\partial_{\theta} \epsilon$ (colour coded by purple/green; Fig. 1b) add a phase difference of π between the effective currents at the corners of this target. The section ‘From information sources to information radiation patterns’ shows that this phase difference will play an important role in explaining the far-field information radiation patterns of symmetric particles in free space.

Remarkably, the continuity equation (5) encapsulates the fact that the FI flux is a conserved quantity, not only for waves propagating through free space but also throughout those parts of a medium unaffected by a variation in the parameter of interest θ . In systems with absorption (as modelled by a complex permittivity), not only energy but also FI gets attenuated by an additional absorption term $\sigma^{\text{abs}} = -2\hbar^{-1} \text{Im}(\epsilon) |\partial_{\theta} \mathbf{E}_{\omega}|^2$. As a consequence, all the FI flux created by information sources either propagates out of the system or gets annihilated by information sinks such as regions that are dissipative or that depend on θ .

To locate the sources of FI in a system, it is convenient to introduce a small perturbation to θ and observe how the scattering landscape changes as a result. For example, in Fig. 1, rotating the target object shows that the orientation information is generated most strongly near the corners of that object. However, we highlight that the introduction of such perturbations only serves to visualize the FI flow and its sources; indeed, even without such perturbations, the scattered wave contains FI about all the parameters of a system with which the wave has interacted. To access the FI, an estimator of the parameter θ is required, which comes with the complication that it is generally only valid for a specific system configuration. Although an estimator can, thus, be constructed based on additional system information¹², an explicit variation of θ provides direct access to the estimator without any prior knowledge of the system²⁰.

Experimental visualization

To experimentally demonstrate that the FI flux is also accessible, we present below the corresponding measurements in a microwave setup. The electromagnetic fields are generated and measured here using antennas that give us direct access to the FI flux in the near and far

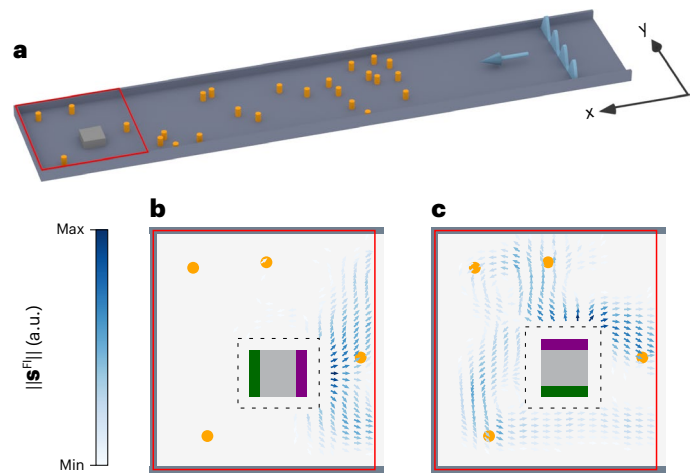


Fig. 2 | FI flow in a microwave setup. **a**, Sketch of the experimental setup. We depict the Teflon scatterers as orange cylinders and the metallic target scatterer as a light grey cube. Waves are injected from the right side as indicated by the light blue wavefront. The near-field measurement area is highlighted in red. **b**, FI flux (blue arrows) for the case that the estimated parameter $\theta = x_{\text{scat}}$ is the horizontal position of the grey target object. **c**, FI flux corresponding to its vertical position $\theta = y_{\text{scat}}$. The area around the target is shown for the case that an input state is injected (at 6.45 GHz), which maximizes the FI at the output for the given parameter θ . In accordance with our predictions, one clearly observes that the FI emerges from the purple and green regions where the refractive index changes when θ is perturbed. The dashed line indicates where the proximity of the target object prohibits near-field measurements.

fields. To simplify the setup and reduce complexity, we employ a flat rectangular waveguide that is closed by a metal plate on the left side (Fig. 2a). To create a complex scattering geometry, we introduce Teflon scatterers into the system. Electromagnetic waves are injected from the open lead on the right (blue wave pattern) at a frequency of $f = 6.45$ GHz, allowing for four propagating transverse modes. We consider the FI fluxes corresponding to the horizontal (x_{scat}) and vertical (y_{scat}) positions of a rectangular metallic target scatterer (light grey cuboid), embedded inside a set of 25 small circular Teflon scatterers (orange cylinders). In the same way as in previous studies^{32–34}, the electric field is measured in the near field around the target (red frame), once before and after shifting the target slightly along the x or y axis, allowing us to construct the FI flux for the relevant parameters $\theta = x_{\text{scat}}$ or $\theta = y_{\text{scat}}$ using finite differences. A more detailed description of the experimental setup is given in the ‘Methods’ section.

In the experimental results shown in Fig. 2b, we have used the FI operator to inject the optimal incident state that maximizes the collected FI in the far field on the right side of the waveguide²⁰. Our results clearly show how the flux of FI on x_{scat} (blue arrows) emerges from the target scatterer’s right-hand side and propagates towards the far field. This confirms that those parts of the target that change under the variation in x_{scat} (Fig. 2b, purple and green regions) act as sources of FI flux. Moreover, the fact that the state with the maximum FI typically originates from the right boundary of the target scatterer (rather than from the left-boundary side) can be attributed to the global absorption in the metallic waveguide walls, resulting in dissipative information loss. Information emanating from the right target boundary, thus, typically propagates along shorter paths, which are more efficient in transferring information to the waveguide output. For comparison, Fig. 2c shows the flux of FI corresponding to the vertical position y_{scat} of the target object. Once again, using the optimal incident state, we observe that the flux mainly originates from the upper side of the target object, which constitutes one of the two possible sources of FI (Fig. 2c, purple and green regions).

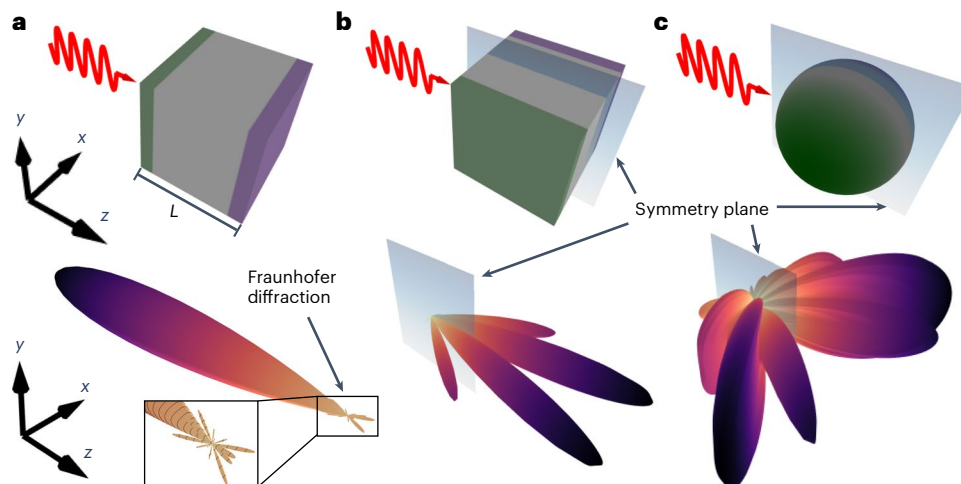


Fig. 3 | FI radiation patterns. **a, b**, A weakly scattering cube with side length $L = 1.4\lambda$ is illuminated by a plane wave (red line) propagating along the positive z direction to estimate the cube's position along the z and x directions, respectively (top panels). The FI sources are indicated in purple for $\partial_\theta\epsilon > 0$ and in green for $\partial_\theta\epsilon < 0$. The corresponding angular FI radiation patterns (bottom panels), where larger amplitudes and darker colours indicate stronger radiation in a specific direction. The radiation patterns show strong similarities to the

interference of Fraunhofer diffraction patterns emanating from two rectangular apertures (**a**) and from a double slit (**b**). Due to destructive interference between the π -phase-shifted sources in green and purple, no information is radiated in the symmetry plane indicated in **b** by the light blue surface. **c**, A silica sphere (top), illuminated by a Gaussian beam with a numerical aperture of 0.1. Corresponding radiation pattern of FI with respect to the sphere's x position (bottom). Just as in **b**, no information is radiated in the symmetry plane.

From information sources to information radiation patterns

So far, the π -phase differences added to the information sources by $\partial_\theta\epsilon$ (Fig. 2b,c, purple and green regions) seemingly did not play a substantial role in the way FI is transferred from the near to the far field. This can be attributed to the spatially asymmetric scattering induced by the disordered environment, scrambling the phases of the effective currents. We will now demonstrate that for symmetric particles in free space, on the contrary, these π -phase shifts are crucial to understand the structure of the far-field FI flux. The structure of such 'information radiation patterns' is of particular interest in levitated optomechanics, as it determines the optimal placement of a detector to provide efficient feedback on a levitated particle^{29,35} (when placing the detector at a position in which no FI on a specific parameter flows, no feedback cooling of this degree of freedom is possible).

Building on the far-field description of FI²⁰, previous studies^{36–38} have demonstrated the utility of FI in identifying optimal incident states for particle cooling and micro-manipulation. However, as we will now explicitly demonstrate, the added benefit of a near-field description of FI allows us to understand the shape of these FI radiation patterns, connecting our theory to antenna engineering and diffraction theory. Let us first consider, for simplicity, a weakly scattering dielectric cube (side length L , $\epsilon = 1.001\epsilon_0$) illuminated by a plane wave $\mathbf{E}_{\omega,0} = e^{ikz}\mathbf{e}_y$ ($\lambda = 1.4L$) that propagates along the z axis. The parameter of interest here is the position of the particle along the z direction (Fig. 3a). As predicted by our theory, the sources of FI manifest at the front and back sides of the cube, delineated by purple and green rectangles, where the colours indicate the sign of $\partial_\theta\epsilon$: purple for positive (front side) and green for negative (back side). Due to the weak scattering of the target, we can approximate the effective electric currents $\mathbf{j}_{\text{eff}}^e = -4i\hbar^{-1}(\partial_\theta\epsilon)\mathbf{E}_\omega$ that induce FI (as introduced below equation (5)) by replacing the full field \mathbf{E}_ω with the incident field $\mathbf{E}_{\omega,0}$. Each one of the two effective currents associated with the rectangular front and back sides of the target is then analogous to the effective electric current one would obtain for the diffraction at a rectangular aperture³⁹. Correspondingly, we find an FI radiation pattern (Fig. 3a, bottom) akin to the interference pattern of two independent rectangular antennas positioned at the sources' locations. Although the destructive interference of the sources results

in the suppression of the forward radiation of information, Fraunhofer-like diffraction lobes are observed in the other directions (Supplementary Section 3.1).

Next, we displace the cube along the x direction (Fig. 3b), which shifts the FI sources to plates (coloured in blue and purple) located on the sides of the cube along the x direction. The different signs of $\partial_\theta\epsilon$ on these plates imparts a reflection anti-symmetry on the effective currents, not only resulting in destructive interference of the information flow in the direct forward transmission but in all the directions along the symmetry plane (indicated by the blue plane; Supplementary Section 3.4). From the perspective of the incident field, the two plates look like thin slits, which explains the similarity of the lobes in the FI radiation pattern to the diffraction patterns at a double slit (Supplementary Section 3.1).

These observations extend to more experimentally relevant scenarios, such as silica spheres illuminated by a Gaussian beam (Fig. 3c) for which an analogous anti-symmetry suppresses information about any of its positional parameters radiating along the forward scattering direction (Supplementary Section 3.2).

Information density as a local property of waves

In the next step, we investigate the dynamical process of FI generation at a target object and its storage within the scattered wave. For this purpose, we extend our framework from the time-independent continuity equation (5) to the temporal domain. To be specific, we consider quasi-monochromatic wave packets, denoted as $\mathbf{E} = \text{Re}[\mathbf{E}_\omega(\mathbf{r}, t)e^{-i\omega t}]$, where the complex amplitude \mathbf{E}_ω slowly varies with time and thereby determines the wave-packet's envelope function. In analogy to the energy density, we introduce the FI density as $u^{\text{FI}} = (\hbar\omega)^{-1}(\epsilon|\partial_\theta\mathbf{E}_\omega|^2 + \mu_0|\partial_\theta\mathbf{H}_\omega|^2)$, which provides the missing term to complete the fully time-dependent continuity equation:

$$\nabla \cdot \mathbf{S}^{\text{FI}} + \partial_t u^{\text{FI}} = \sigma^{\text{FI}}. \quad (6)$$

This 'Poynting theorem' for FI contains the FI flux \mathbf{S}^{FI} and sources σ^{FI} , as already defined for the time-independent equation (5). The determined FI density u^{FI} describes the local density of FI of the electromagnetic field at any given location.

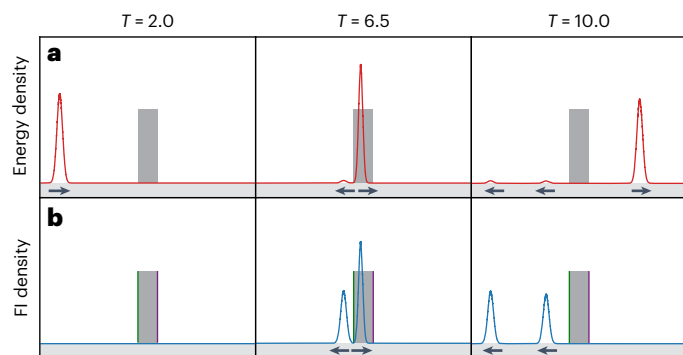


Fig. 4 | FI content of a wave packet. A one-dimensional wave packet closely centred around a frequency ω scatters off a dielectric (grey rectangle), whose position is the parameter of interest. **a**, Energy density envelope (red) at times $T = 2.0, 6.5$ and 10.0 (arbitrary units). The black arrows indicate the direction of motion of the wave packet. **b**, FI density (blue) at the same times. Information is created at the sources located at the two sides of the scatterer (purple and green). Most of the energy is transmitted, whereas the information is solely flowing into the reflection channel.

To illustrate these quantities, Fig. 4 shows the propagation of a one-dimensional wave packet scattering off a barrier (refractive index, $n \approx 1.41$). The FI that we consider here corresponds to the x position of the barrier (grey rectangle), such that the information sources and sinks are located at the very left and right sides of the barrier (purple and green bars). In Fig. 4a, we plot the energy envelope of the wave packet entering from the left and scattering off the barrier. Although a small part of the energy is reflected at the barrier, most of it is transmitted. For comparison, Fig. 4b depicts the FI density stored in the wave. In particular, the incoming wave packet does not carry any FI before hitting the barrier. When the wave packet overlaps with the left side of the barrier, two pulses of FI are created (Fig. 4b, middle). Remarkably, when the same happens at the overlap of the wave packet with the right side of the barrier, the right-moving FI wave packet created at this moment destructively interferes with the right-moving packet created earlier at the left side of the barrier (due to a phase shift of π). This reflects the fact that the transmitted wave is entirely invariant with respect to the barrier position, such that no FI can reach the transmission channel. As a result, all FI created in this simple scattering problem is reflected to the source, mostly in the form of the two FI wave packets shown in Fig. 4b (right) (further back-reflected peaks exist, but are very small in amplitude). A video containing a numerical animation of this scattering problem is provided in Supplementary Video 1. These observations demonstrate that energy and information can propagate in opposite ways, which can be used to hide information from an eavesdropper even in complex scattering environments (Supplementary Section 4). Figure 4 also highlights that those parts of the system sensitive to θ do not necessarily act as sources of information, but can also act as information sinks.

FI in the near field

To substantiate the validity of our expressions for the FI density inside a complex scattering system (that is, in the near field), we present an independent analysis in which a collection of N atoms located near the position \mathbf{r}_0 is used as a local probe of the FI in the electromagnetic wave that can ionize these atoms. In analogy to the derivations provided in ref. 40, where the transition rate and thus the energy transfer to the atoms is given by the energy density in the transverse part of the electric field, in Supplementary Section 5, we provide a calculation for the corresponding transfer of FI, $\mathcal{J}_e(\theta)$, to the ionization probability of electrons in this process. We find that, indeed, the obtained rate of FI transferred in the ionization process is directly proportional to the FI

density contained in the transverse electric field $u_{\mathbf{E}^T}^{\text{FI}} = (\hbar\omega)^{-1} |\partial_\theta \mathbf{E}_\omega^T|^2 \epsilon_0$ in analogy to the transfer of energy:

$$\mathcal{J}_e(\theta) \leq 2N\eta u_{\mathbf{E}^T}^{\text{FI}}(\mathbf{r}_0). \quad (7)$$

The equality in this relation holds if the phase of \mathbf{E}_ω^T does not change with θ (for example, by adding a reference beam with a suitable phase so that all of the information is contained in the intensity rather than in the phase of the field \mathbf{E}_ω^T at \mathbf{r}_0). The factor η characterizes the average ionization/detection efficiency⁴⁰ of the atoms. Through this relation, we can assign a practical meaning to our expression for the transversal electric part of the FI density, even in the context of light–matter interaction.

An interesting observation in this setting is the fact that although photodetectors can only access the transversal part of the electric field, the continuity equation (6) shows that part of the FI is stored even in the longitudinal-field components. These longitudinal components arise inside or in close proximity to the matter that the fields interact with, but rapidly fall off with a scaling of $\propto r^{-6}$, where r represents the distance to the matter (Supplementary Section 6). Deviations from our classical analysis may arise when interactions of the above atomic detectors with the scattering system cannot be neglected anymore or a full quantum treatment becomes necessary⁴¹. As long as the system–detector interaction stays weak and the rotating-wave approximation remains valid, we can show that the FI density of the transverse fields, integrated over all of space, is equal to the total amount of quantum FI contained in the photon field at each point in time (Supplementary Section 7).

Conclusion

In conclusion, we introduce here a framework to describe and evaluate the density and flow of FI in electromagnetic scattering problems. In analogy to the seminal Poynting theorem that describes the conservation of energy in the propagation of waves even through highly complex environments, we formulate a corresponding continuity equation for the creation, annihilation and conservation of FI. Our approach holds substantial potential for advancing the understanding of imaging systems and precision measurements. As a promising example, we mention the field of levitated optomechanics, where great interest has recently been focused on measuring the positions of individual particles as fast and accurately as possible to cool these particles to their motional ground states^{42–45}. In this context, it is important to know in which direction the information on a particle's position is radiated for optimal detection^{35,46}. Our approach provides the theoretical basis to quantify such FI radiation patterns for scattering particles of arbitrary shape and size, even in the presence of multiple scattering between particles. Although our experimental results were specifically obtained in the microwave regime, the theoretical framework we have developed is applicable across the entire electromagnetic spectrum and can be extended to media with more complex constitutive relations. Considering other wave equations with a similar mathematical structure, our theory could serve as a framework to analyse FI propagation in a broad range of different physical contexts, such as ultrasound, seismic or quantum matter waves.

Online content

Any methods, additional references, Nature Portfolio reporting summaries, source data, extended data, supplementary information, acknowledgements, peer review information; details of author contributions and competing interests; and statements of data and code availability are available at <https://doi.org/10.1038/s41567-024-02519-8>.

References

1. Poynting, J. H. XV. On the transfer of energy in the electromagnetic field. *Phil. Trans. R. Soc.* **175**, 343–361 (1884).
2. Slepian, J. Energy flow in electric systems—the Vi energy-flow postulate. *Trans. Am. Inst. Electr. Eng.* **61**, 835–841 (1942).

3. Geyi, W., Jarmuszewski, P. & Qi, Y. The Foster reactance theorem for antennas and radiation Q. *IEEE Trans. Antennas Propag.* **48**, 401–408 (2000).
4. Hawthorne, E. Flow of energy in synchronous machines. *Trans. Am. Inst. Elect. Eng. Part 1* **73**, 1–10 (1954).
5. Kelley, M., Knudsen, D. & Vickrey, J. Poynting flux measurements on a satellite: a diagnostic tool for space research. *J. Geophys. Res.: Space Phys.* **96**, 201–207 (1991).
6. Di Renzo, M., Danufane, F. H. & Tretyakov, S. Communication models for reconfigurable intelligent surfaces: from surface electromagnetics to wireless networks optimization. *Proc. IEEE* **110**, 1164–1209 (2022).
7. Moreira, A. et al. A tutorial on synthetic aperture radar. *IEEE Geosci. Remote Sens. Mag.* **1**, 6–43 (2013).
8. Webb, A. *Introduction to Biomedical Imaging* (John Wiley & Sons, 2022).
9. Taylor, R. W. & Sandoghdar, V. Interferometric scattering microscopy: seeing single nanoparticles and molecules via Rayleigh scattering. *Nano Lett.* **19**, 4827–4835 (2019).
10. Abbott, B. P. et al. Observation of gravitational waves from a binary black hole merger. *Phys. Rev. Lett.* **116**, 061102 (2016).
11. Lazarev, G. et al. *Optical Imaging and Metrology: Advanced Technologies* (Wiley-VCH, 2012).
12. Balzarotti, F. et al. Nanometer resolution imaging and tracking of fluorescent molecules with minimal photon fluxes. *Science* **355**, 606–612 (2017).
13. van Putten, E. G., Lagendijk, A. & Mosk, A. P. Nonimaging speckle interferometry for high-speed nanometer-scale position detection. *Opt. Lett.* **37**, 1070–1072 (2012).
14. Young, G. et al. Quantitative mass imaging of single biological macromolecules. *Science* **360**, 423–427 (2018).
15. Hess, D. W. Introduction to RCS measurements. In *2008 Loughborough Antennas and Propagation Conference* 37–44 (IEEE, 2008).
16. Kay, S. M. *Fundamentals of Statistical Signal Processing* Vol. 1 (Prentice-Hall, 1993).
17. Shechtman, Y., Sahl, S. J., Backer, A. S. & Moerner, W. E. Optimal point spread function design for 3D imaging. *Phys. Rev. Lett.* **113**, 133902 (2014).
18. Tsang, M., Nair, R. & Lu, X.-M. Quantum theory of superresolution for two incoherent optical point sources. *Phys. Rev. X* **6**, 031033 (2016).
19. Barrett, H. H., Myers, K. J. & Rathee, S. Foundations of image science. *Med. Phys.* **31**, 953 (2004).
20. Bouchet, D., Rotter, S. & Mosk, A. P. Maximum information states for coherent scattering measurements. *Nat. Phys.* **17**, 564–568 (2021).
21. Bouchet, D., Carminati, R. & Mosk, A. P. Influence of the local scattering environment on the localization precision of single particles. *Phys. Rev. Lett.* **124**, 133903 (2020).
22. Boffety, M., Allain, M., Sentenac, A., Massonneau, M. & Carminati, R. Analysis of the depth resolution limit of luminescence diffuse optical imaging. *Opt. Lett.* **33**, 2290–2292 (2008).
23. Pinel, O., Jian, P., Treps, N., Fabre, C. & Braun, D. Quantum parameter estimation using general single-mode Gaussian states. *Phys. Rev. A* **88**, 040102 (2013).
24. Fiderer, L. J., Fraise, J. M. E. & Braun, D. Maximal quantum Fisher information for mixed states. *Phys. Rev. Lett.* **123**, 250502 (2019).
25. Bouchet, D. & Bossy, E. Temporal shaping of wave fields for optimally precise measurements in scattering environments. *Phys. Rev. Res.* **5**, 013144 (2023).
26. Lu, X.-M., Wang, X. & Sun, C. P. Quantum Fisher information flow and non-Markovian processes of open systems. *Phys. Rev. A* **82**, 042103 (2010).
27. Bon, P. & Cognet, L. On some current challenges in high-resolution optical bioimaging. *ACS Photonics* **9**, 2538–2546 (2022).
28. Young, G. & Kukura, P. Interferometric scattering microscopy. *Annu. Rev. Phys. Chem.* **70**, 301–322 (2019).
29. Gonzalez-Ballester, C., Aspelmeyer, M., Novotny, L., Quidant, R. & Romero-Isart, O. Levitodynamics: levitation and control of microscopic objects in vacuum. *Science* **374**, 3027 (2021).
30. Liu, F., Liu, Y.-F., Li, A., Masouros, C. & Eldar, Y. C. Cramér-Rao bound optimization for joint radar-communication beamforming. *IEEE Trans. Signal Process.* **70**, 240–253 (2021).
31. Jackson, J. D. Classical electrodynamics. *Am. J. Phys.* **67**, 841–842 (1999).
32. Pichler, K. et al. Random anti-lasing through coherent perfect absorption in a disordered medium. *Nature* **567**, 351–355 (2019).
33. Ambichl, P. et al. Focusing inside disordered media with the generalized Wigner-Smith operator. *Phys. Rev. Lett.* **119**, 033903 (2017).
34. Horodyski, M. et al. Optimal wave fields for micromanipulation in complex scattering environments. *Nat. Photon.* **14**, 149–153 (2020).
35. Maurer, P., Gonzalez-Ballester, C. & Romero-Isart, O. Quantum theory of light interaction with a Lorenz-Mie particle: optical detection and three-dimensional ground-state cooling. *Phys. Rev. A* **108**, 033714 (2023).
36. Hüpfl, J. et al. Optimal cooling of multiple levitated particles through far-field wavefront shaping. *Phys. Rev. Lett.* **130**, 083203 (2023).
37. Hüpfl, J. et al. Optimal cooling of multiple levitated particles: theory of far-field wavefront shaping. *Phys. Rev. A* **107**, 023112 (2023).
38. Horodyski, M., Reiter, T., Kühmayer, M. & Rotter, S. Tractor beams with optimal pulling force using structured waves. *Phys. Rev. A* **108**, 023504 (2023).
39. Visser, H. J. *Antenna Theory and Applications* (John Wiley & Sons, 2012).
40. Mandel, L. & Wolf, E. *Optical Coherence and Quantum Optics* (Cambridge Univ. Press, 1995).
41. Kienesberger, L., Juffmann, T. & Nimmrichter, S. Quantum limits of position and polarizability estimation in the optical near field. *Phys. Rev. Res.* (in the press).
42. Tebbenjohanns, F., Mattana, M. L., Rossi, M., Frimmer, M. & Novotny, L. Quantum control of a nanoparticle optically levitated in cryogenic free space. *Nature* **595**, 378–382 (2021).
43. Piotrowski, J. et al. Simultaneous ground-state cooling of two mechanical modes of a levitated nanoparticle. *Nat. Phys.* **19**, 1009–1013 (2023).
44. Delić, U. et al. Cooling of a levitated nanoparticle to the motional quantum ground state. *Science* **367**, 892–895 (2020).
45. Rudolph, H., Delić, U. C. V., Aspelmeyer, M., Hornberger, K. & Stickler, B. A. Force-gradient sensing and entanglement via feedback cooling of interacting nanoparticles. *Phys. Rev. Lett.* **129**, 193602 (2022).
46. Tebbenjohanns, F. et al. Optimal orientation detection of an anisotropic dipolar scatterer. *Phys. Rev. A* **105**, 053504 (2022).

Publisher's note Springer Nature remains neutral with regard to jurisdictional claims in published maps and institutional affiliations.

Springer Nature or its licensor (e.g. a society or other partner) holds exclusive rights to this article under a publishing agreement with the author(s) or other rightsholder(s); author self-archiving of the accepted manuscript version of this article is solely governed by the terms of such publishing agreement and applicable law.

© The Author(s), under exclusive licence to Springer Nature Limited 2024

Methods

Experiment

The measurement setup and experimental methods we present in this section are inspired by refs. 32–34.

Setup. A cross section of the experimental setup is shown in Extended Data Fig. 1. We work with a rectangular aluminium waveguide of length 1.103 m (x direction) and inner width of 0.100 m (y direction). The system is slightly higher in the near-field measurement area (11 mm) than in the other regions (8 mm). Although the waveguide is closed with a metallic wall on the left, we use an absorbing material to imitate an open lead on the right. Within the system, we randomly place 25 cylindrical Teflon scatterers of radius 2.55 mm (orange rectangles). Amidst the resulting complex scattering layer, we place a cuboid metallic target scatterer of side length 2 cm (dark grey rectangle). We use a pin in the bottom plate of the waveguide to fix the position of the target scatterer, which allows us to execute a precise perturbation of θ .

To determine the microwave field for a given incoming state, we measure the transmission from port 2 to port 1 of a vector network analyser (VNA) at different positions in the system (note that the transmission is a unitless quantity since it is always determined relative to what we send into the system at the calibration point). Port 1 of the VNA is connected to a probe antenna, which we position using three step motors (not shown). Port 2 is connected to four injection antennas via a power splitter and four IQ modulators. Both probe and injection antennas couple weakly to the system. Although the measured transmission is proportional to the z component of the electric field, we can only determine the latter up to an unknown constant factor since the exact coupling strengths of the two antennas is unknown.

The incoming state is controlled by choosing the relative phase and the attenuation of the IQ modulators (see the ‘Scattering matrix and wavefront engineering’ section). We can measure both far field (via holes in the top plate) and near field (using a movable part of the top plate with an integrated antenna). As opposed to the measurement holes, the movable top plate allows us to probe the microwave field at arbitrarily close positions, enabling us to calculate the spatial derivatives in the expression for the FI flux.

We measure the microwave transmission spectra in the near-field measurement area on a grid of 39×39 evenly spaced points that are 2.5 mm apart in the x and y directions. Note that we could not perform measurements above the target scatterer since it touches the top plate. To evaluate the spatial gradients in the expression of the FI flux on this grid, we use central finite differences. At the grid edges, we use forward/backward finite differences. The finite differences with respect to θ can be computed by performing the above measurement for the unperturbed and perturbed systems and subtracting the microwave fields.

Frequency range and smoothing. In rectangular waveguides, only $TE_{m,n}$ and $TM_{m,n}$ modes exist. Furthermore, each TE/TM mode has a cut-off frequency, given by

$$\omega_{\text{cut-off}}^2(m, n) = \frac{1}{\epsilon\mu} \left(\left(\frac{m\pi}{d_y} \right)^2 + \left(\frac{n\pi}{d_z} \right)^2 \right), \quad (8)$$

below which they are evanescent and decay exponentially³¹. Here $d_y = 10$ cm/ $d_z = 8$ mm corresponds to the extent of the waveguide in the y/z direction. Note that for frequencies below $c/(2d_z) = 18.74$ GHz, only modes with $m = 0$ are non-evanescent.

We measure the transmission between port 2 and port 1 of the VNA at 2,501 equally spaced frequency points in the interval $f \in [6.0 \text{ GHz}, 7.5 \text{ GHz}]$, ensuring that $TE_{0,n}$, $n \leq 4$, are the only propagating modes. We, thus, avoid the z dependence of the scalar microwave field $\psi \propto E_z(x, y)$. Furthermore, we can control all the degrees of freedom using the four injection antennas. To reduce the measurement noise, we apply a triangular filter of width 7 to the transmission spectra, that is,

$$T(n_f) = \frac{1}{16} (\tilde{T}(n_f - 3) + 2\tilde{T}(n_f - 2) + 3\tilde{T}(n_f - 1) + 4\tilde{T}(n_f) + 3\tilde{T}(n_f + 1) + 2\tilde{T}(n_f + 2) + \tilde{T}(n_f + 3)),$$

where $T(n_f)/\tilde{T}(n_f)$ denotes the smoothed/measured signal at the frequency point n_f , where $4 < n_f < 2,498$.

Far-field wavefunction. As opposed to the near field, the far field in our setup has a simple mathematical form⁴⁷:

$$\psi(x, y) = \sum_{n=1}^N \frac{1}{\sqrt{k_n^x}} \chi_n(y) [c_n^{\text{in}} e^{ik_n^x x} + c_n^{\text{out}} e^{-ik_n^x x}], \quad (9)$$

where $N = \left\lfloor \frac{d_y k}{\pi} \right\rfloor = 4$ denotes the number of open (flux-carrying) modes, and $c_n^{\text{in}}/c_n^{\text{out}}$ denote the coefficients of the wavefront going in/coming out of the system. We further defined the transverse mode profiles as

$$\chi_n(y) = \sqrt{\frac{2}{d_y}} \sin\left(\frac{n\pi y}{d_y}\right), \quad (10)$$

$$\int_0^{d_y} \chi_n(y) \chi_{n'}(y) dy = \delta_{nn'}.$$

We can determine $\mathbf{c}^{\text{in}} = (c_1^{\text{in}}, c_2^{\text{in}}, \dots, c_N^{\text{in}})^T$ and $\mathbf{c}^{\text{out}} = (c_1^{\text{out}}, c_2^{\text{out}}, \dots, c_N^{\text{out}})^T$ at a fixed frequency and for given IQ modulator settings by measuring the microwave field in all 6×19 top-plate holes and performing a fit to equation (9). More specifically, we first compute

$$c_n(x) := c_n^{\text{in}} e^{ik_n^x x} + c_n^{\text{out}} e^{-ik_n^x x}$$

at each x position with the help of SciPy’s `curve_fit` function⁴⁸. Then, we perform a multivariate linear regression using the scikit-learn library to obtain \mathbf{c}^{in} and \mathbf{c}^{out} (ref. 49). Extended Data Fig. 2 shows the result of such a fit for $f = 6.45$ GHz and the following IQ modulator settings:

$$\text{IQM}_0 \{ \text{attenuation, } 0 \text{ dB; phase, } 0 \},$$

$$\text{IQM}_{i \neq 0} \{ \text{attenuation, } 40 \text{ dB; phase, } 0 \},$$

that is, the zeroth injection antenna is fully illuminated, whereas the remaining antennas are on the maximum attenuation. We depict the real part of the measured transmission and the far-field wavefunction from equation (9), where we plug in the \mathbf{c}^{in} and \mathbf{c}^{out} values from the fit. Since the latter agree well, we conclude that the wave propagates freely in the far field and we can characterize it with the \mathbf{c}^{in} and \mathbf{c}^{out} values from the fit.

Scattering matrix and wavefront engineering. The coefficients of the incoming waves \mathbf{c}^{in} are related to the coefficients of the outgoing waves \mathbf{c}^{out} via the scattering matrix S . We can, thus, determine the latter by measuring the \mathbf{c}^{out} value corresponding to four linearly independent \mathbf{c}^{in} values and by solving the system of linear equations. By illuminating the injection antennas one after the other and maximally attenuating the remaining ones, we can easily identify the required four linearly independent wavefronts.

Since the scattering system is linear, we can inject a desired microwave state into it once we know the four linearly independent \mathbf{c}^{in} values. In this way, we can produce any superposition of the latter by choosing the attenuation and the relative phase of the IQ modulators.

Numerical methods

One-dimensional time-dependent simulations. The time-dependent simulations are performed for scalar Maxwell equations using the

finite-difference method and outgoing boundary conditions. For convenience, we set $c = 1$ and all other units to 1. The incident wave packet is given by

$$f(x, t) = f_0 e^{-(t-x)^2/\tau} \sin(\omega(t-x)) \quad (11)$$

for $\tau = 0.2$ and $\omega = 500$. The scatterer barrier considered in Fig. 4 has a dielectric constant of $\epsilon = 2\epsilon_0$, a width of $w = 1$ and the left side is located at $x = 5$.

Three-dimensional free-space simulations. The three-dimensional free-space simulations are done using the Green dyadic method implemented by the pyGDM2 Python library⁵⁰.

Data availability

Source data are provided with this paper. All other data that support the plots within this paper and other findings of this study are available from the corresponding authors on reasonable request.

Code availability

The code used for the radiation patterns is publicly available via the pyGDM2 library⁵⁰. The one-dimensional time-dependent finite-difference code is available from J.H. (jakob.huepfl@tuwien.ac.at) on reasonable request.

References

47. Rotter, S. & Gigan, S. Light fields in complex media: mesoscopic scattering meets wave control. *Rev. Mod. Phys.* **89**, 015005 (2017).
48. Virtanen, P. et al. SciPy 1.0: fundamental algorithms for scientific computing in Python. *Nat. Methods* **17**, 261–272 (2020).
49. Pedregosa, F. et al. Scikit-learn: machine learning in Python. *J. Mach. Learn. Res.* **12**, 2825–2830 (2011).
50. Wiecha, P. R. pyGDM—a python toolkit for full-field electro-dynamical simulations and evolutionary optimization of nanostructures. *Comp. Phys. Commun.* **233**, 167–192 (2018).

Acknowledgements

We thank C. Gonzalez-Ballester, O. Romero-Isart and M. Weimar for helpful discussions. We also thank M. Kühmayer for providing parts of the simulation code. Support from the Austrian Science Fund (FWF) under project no. P32300 (WAVELAND) to J.H. and S.R. and from TU Wien's KUWI scholarship to F.R. is gratefully acknowledged. The computational results presented were achieved using the Vienna Scientific Cluster (VSC).

Author contributions

J.H. set up the theoretical framework and performed the analytical calculations under the supervision of D.B., L.M.R. and S.R. F.R. performed the experiment together with J.L., under the supervision of U.K. The numerical calculations were carried out together by J.H., F.R. and L.M.R. S.R. proposed the project. J.H. and S.R. wrote the manuscript with the assistance of F.R. and with input from all authors.

Competing interests

The authors declare no competing interests.

Additional information

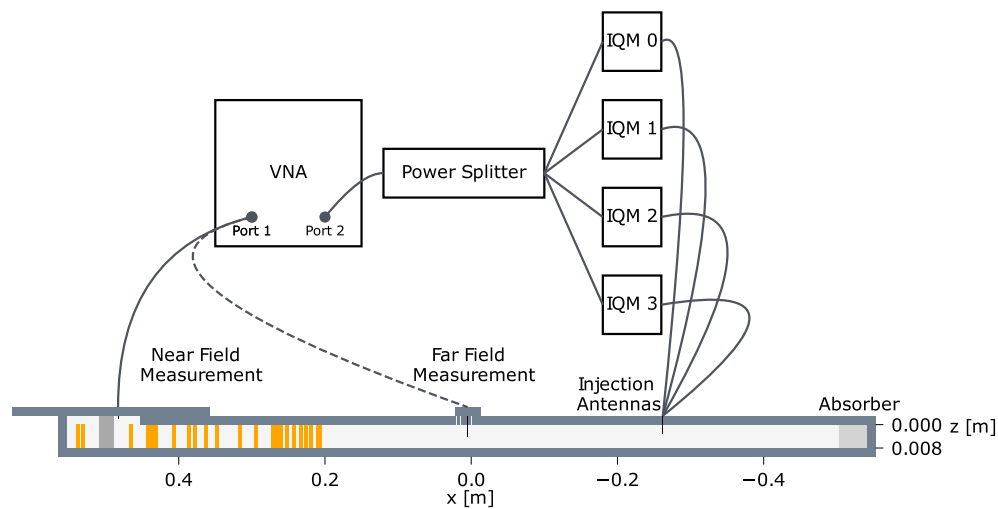
Extended data is available for this paper at <https://doi.org/10.1038/s41567-024-02519-8>.

Supplementary information The online version contains supplementary material available at <https://doi.org/10.1038/s41567-024-02519-8>.

Correspondence and requests for materials should be addressed to Ulrich Kuhl or Stefan Rotter.

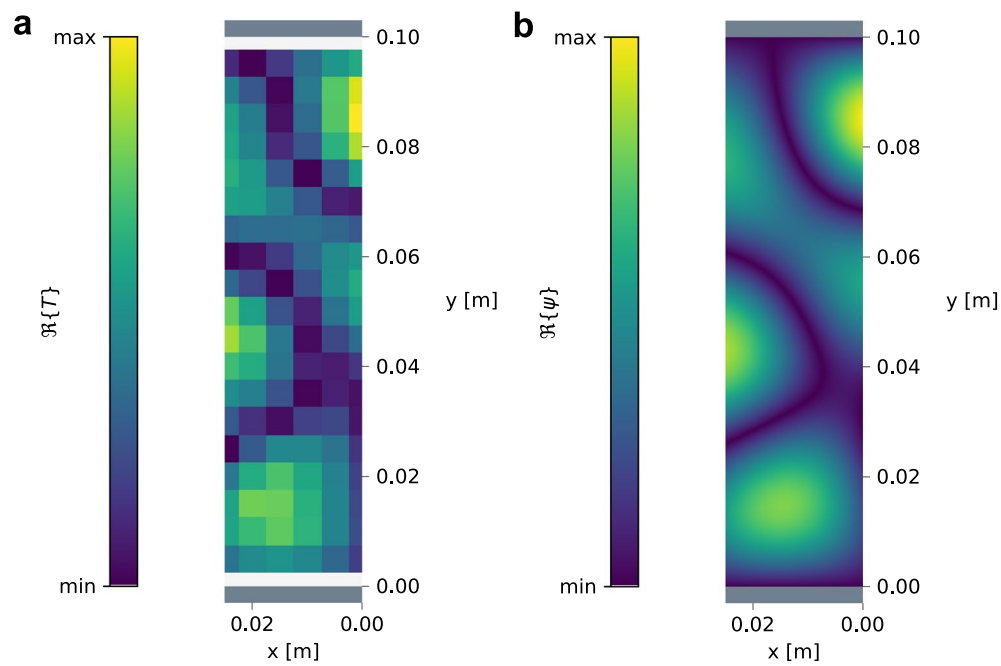
Peer review information *Nature Physics* thanks Daniele Faccio and the other, anonymous, reviewer(s) for their contribution to the peer review of this work.

Reprints and permissions information is available at www.nature.com/reprints.



Extended Data Fig. 1 | Experimental setup. Cross section of the experimental setup in the x - z plane during a far field (dotted line) and a near field (solid line) measurement. We choose the aspect ratio of the axes scaling as 1:4 (x -scale: z -scale) for better visibility. To imitate an infinitely long system, we place an absorber on the right side. On the left side, the waveguide is closed with a metallic wall. Using Teflon (orange rectangles, 8 mm high) and metallic (dark gray

rectangle, 11 mm high) scatterers, we create a complex scattering environment on the left side. We connect the probe antenna to port 1 of the VNA and attach it to three step motors (not shown), which we use to position it. To port 2, we connect the four injection antennas via a power splitter and four IQ modulators. Note that the waveguide is higher in the near field measurement area (11 mm) than in the other regions (8 mm).



Extended Data Fig. 2 | Far field wavefunction. Comparison of the measured transmission from port 2 to port 1 of the VNA at $f = 6.45$ GHz (**a**) and the wavefunction from Eq. (2), where we plug in the \mathbf{c}^{in} and \mathbf{c}^{out} from the fit (**b**). We illuminate the 0th injection antenna fully while attenuating the remaining antennas maximally and show the real part of the transmission/wavefunction.